Heliyon 9 (2023) e22169

Contents lists available at ScienceDirect

Heliyon

journal homepage: www.cell.com/heliyon

Review article

Review on corrosion of alloys for application in supercritical carbon dioxide brayton cycle

Ziyuan Xu [a], Yingying Yang [a,b,*], Shijie Mao [a], Weidong Wu [a], Qiguo Yang [a]

[a] School of Energy and Power Engineering, University of Shanghai for Science and Technology, Shanghai, 200093, China
[b] Shanghai Key Laboratory of Multiphase Flow and Heat Transfer in Power Engineering, Shanghai, 200093, China

ARTICLE INFO

Keywords:
Supercritical carbon dioxide (S–CO_2)
Brayton cycle
Oxidation
Carburization
Superalloy

ABSTRACT

The supercritical carbon dioxide (S–CO_2) Brayton cycle is considered a promising power generation system because of its high efficiency, simple layout, and compact configuration. Furthermore, it is applicable to thermal and nuclear power generation. Because the key end equipment of this system is exposed to a high-temperature and high-pressure S–CO_2 environment for a long duration, the high-temperature corrosion resistance of this equipment has been investigated extensively. This paper provides a review of recent studies pertaining to the corrosion behavior of candidate materials for high-temperature components in the S–CO_2 Brayton cycle system. Additionally, the effects of internal microstructure, metal element content and external environment (temperature, pressure, impurities, etc.) on the corrosion behavior of alloys, including oxidation and carburizing corrosion are analyzed. Problems pertaining to the corrosion behavior of candidate materials are highlighted, and possible areas for future research are proposed.

1. Introduction

As global energy demand continues to increase, the energy conversion efficiency of power generation systems must be improved urgently. Currently, the most typically used power generation cycles include the supercritical water-steam Rankine cycle, organic Rankine cycle and supercritical Brayton cycle [1]. The Brayton cycle is a widely used power cycle, in which the most typically utilized working fluids include helium [2], air [3], supercritical carbon dioxide (S–CO_2) [4–6] and supercritical nitrous oxide [7]. Among these, the Brayton power cycle with S–CO_2 as the working fluid exhibit significant potential for achieving high thermodynamic efficiency [8]. Several types of S–CO_2 cycles exist. Fig. 1 [9] shows a typical S–CO_2 recompression Brayton cycle system. The cycle segregates the total CO_2 flow into two streams, one that dissipates excess heat to the environment and is compressed, and another that is directly compressed.

CO_2 is an ideal working fluid for Brayton cycles because of, its safety [10], environmental protection [11], good thermal properties [12], and improved system efficiency [13]. Fig. 2 [14] shows the change in thermal efficiency of different systems with the heat source temperature under typical operating conditions. As shown, in the temperature range of 450 °C–650 °C, the efficiency of the S–CO_2 Brayton cycle is higher than that of the helium Brayton and water vapor Rankine cycles; in fact, it reached as high as 47 % at 650 °C. Moreover, compared with other Brayton cycle working fluids, CO_2 can easily reach the critical temperature and pressure; furthermore, it has a higher critical density, thereby rendering the entire system equipment compact. Compared with the conventional steam

* Corresponding author. 516 Jungong Road, Shanghai, 200093, China.
E-mail address: yingyingyang@usst.edu.cn (Y. Yang).

https://doi.org/10.1016/j.heliyon.2023.e22169
Received 16 June 2023; Received in revised form 27 October 2023; Accepted 6 November 2023
Available online 10 November 2023

Rankine cycle system, the *S*–CO_2 Brayton cycle system exhibits an overall scale of only 25 % [15]. Owing to its superior performance, *S*–CO_2 can potentially reduce the cycle cost by more than 20 % compared with the conventional Rankine steam cycle [16,17]. In 1968, Angelino [18] and Feher [19] proposed a closed Brayton cycle using CO_2 as the working fluid. Within an optimal cycle temperature range, the cycle efficiency improved significantly and the component size reduced. The *S*–CO_2 Brayton cycle is applicable to various areas such as nuclear power [20–24] and solar power [25,26]. In fact, the *S*–CO_2 Brayton cycle system has been widely investigated in the fields of thermal, nuclear, and solar power generation, and so forth. For instance, a fourth-generation sodium-cooled fast reactor uses the *S*–CO_2 Brayton cycle, which is a circulatory system with broad application prospects, to replace the conventional steam cycle [27].

However, the hot-end equipment of the *S*–CO_2 Brayton cycle system must remain in a high-temperature and high-pressure *S*–CO_2 environment for a long duration. For example, the turbine inlet temperature and pressure in the design and simulation of a concentrated solar power plant can reach up to 700 °C and 21.6 MPa respectively [28]. The hot-end equipment in the system, which typically operates for more than 20 years, must withstand high-temperature oxidation, various stresses and corrosion, such as carburization and vulcanization. As mentioned previously, the high temperature corrosion resistance of equipment materials is an important factor in determining whether the *S*–CO_2 Brayton cycle can be applied in practice [29]. Therefore, it is of great importance to investigate the corrosion mechanism of alloys in the specific temperature and pressure conditions of *S*–CO_2 Brayton cycle, and it is essential to provides a comprehensive review on recent studies to classify, summary, and analyze the existing findings. But there are few comprehensive review articles on this issue. Although there are a few review articles on the corrosion issues of alloys in *S*–CO_2, such as the review work by R.P. Oleksak [30], it not only lacks a discussion of gas impurities, but also lacks a comprehensive summary of corrosion experiments. Yang et al. [31] provided a more comprehensive overview of the properties of heat-resistant alloys under high-temperature CO_2, including stress corrosion, and explored the influence of impurities. However, a systematic summary of corrosion tests is not provided in these reviews, and the references are not up to date. In addition, for some review articles, their application background is not specific to the *S*–CO_2 Brayton power cycle system we are concerned about. The temperature and pressure ranges investigated in these reviews do not correspond to the *S*–CO_2 Brayton power cycle system. For instance, most of these reviews are focusing on the CCS (Carbon capture and storage) application backgrounds. Which have different temperature and pressure ranges with the *S*–CO_2 Brayton cycle.

To comprehensively present the state of arts in the field of alloy corrosion for *S*–CO_2 Brayton cycle, a more comprehensive review article is indispensable. This study focuses on recent studies that investigate the corrosion behavior of candidate alloys for high-temperature components in *S*–CO_2 Brayton cycle systems. The effects of metal element content, microstructure and external environment (temperature, impurities, pressure, etc.) on the corrosion behavior of alloys are analyzed. Finally, problems to be solved in the current study are highlighted, and future research directions are proposed.

2. Analysis of corrosion behavior characteristics for different alloys

2.1. Candidate materials for hot-end devices

Nuclear power plants used CO_2 to cool their reactors as early as 1956. However, because of the limited operating temperature of the magnesium alloy used in the cladding, the thermal efficiency of the nuclear power plant it low, and severe corrosion is observed in the early stages of operation. Thus, researchers have attempted to identify the appropriate materials for hot-end equipment used in power generation systems [30,32]. Currently, the materials used to manufacture hot-end equipment include stainless steel, heat-resistant steel and high-temperature alloys.

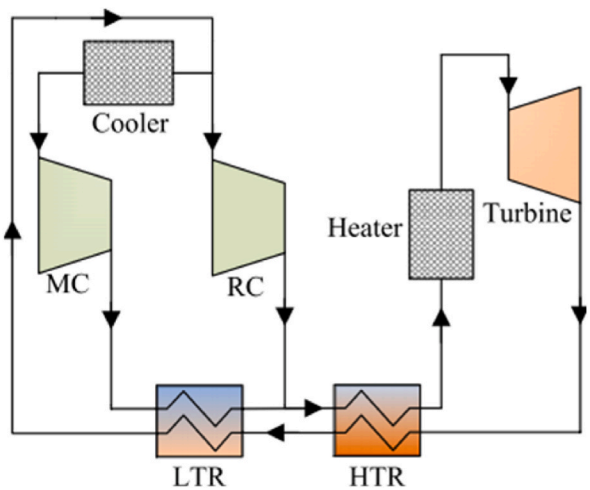

Fig. 1. Recompression *S*–CO_2 cycle [9].

Heat-resistant steels can be classified into martensitic, ferritic, austenitic and precipitation hardening steels based on their structural states. Fig. 3 shows the typical candidate materials and their characteristics. Examples of typical alloys and their applications in high-temperature and high-pressure environments are provided. These alloys are applicable under the specific temperature and pressure conditions in *S*–CO_2 Brayton power cycle, which have potential targeted application. Austenitic steel has been widely used in chemical, petrochemical, marine and nuclear power fields because of its excellent corrosion resistance and mechanical properties [33–37]. Martensitic steel has recently received considerable attention because of its high creep resistance, high thermal conductivity, high radiation resistance and low thermal expansion coefficient [38]. Currently, both types of steel are candidates for hot-end equipment in the *S*–CO_2 Brayton cycle system.

Some studies demonstrated the high corrosion resistance of austenitic steels, which is correlated with chromium content. T91 ferritic-martensitic steel, VM12 ferritic steel, Super 304H, and Sanicro 25 austenitic steel were tested at 650 °C and 15 MPa for 1000 h [39]. A schematic illustration of the system is shown in Fig. 4(a). As shown, the sample was placed in an alumina boat, which was electrically heated to maintain the required temperature and pressure conditions. The results show that the weight gain of Super 304H and Sanicro 25 were lower than those of other samples. Ferritic steel and ferritic-martensitic steel were tested for corrosion in *S*–CO_2 at 550 °C–600 °C [40], and the results showed that ferritic martensitic steel P92 has better corrosion resistance than steel T22, however, at 600 °C, the oxide scale formed on P92 peeled off easily. 4(b) shows a schematic illustration of the experimental setup. The test was performed in a 2 L autoclave. Two high-chromium martensitic steel, 12Cr and 9Cr, and an austenitic stainless steel. 316FR, were used to conduct experiments for 8000 h at 20 MPa and 400 °C–600 °C [41]. The results showed that the weight gain of the 316 F R austenitic steel was significantly lower than that of the martensitic steel.

When applied to the fourth-generation sodium-cooled fast reactor, the temperature and pressure of the *S*–CO_2 Brayton cycle can reach up to 850 °C and 25 MPa, respectively [30]. Heat-resistant steel may not be able to satisfy temperature requirements, in which case superalloys are required. Superalloys generally refer to iron, nickel or cobalt-based austenitic alloy materials, which can withstand large and complex stresses and operate for a long duration at high temperatures exceeding 600 °C. Currently, Ni-based superalloys are the most widely used materials. Some studies showed that Ni-based alloys demonstrate good corrosion resistance in an *S*–CO_2 environment. Lee et al. [42] investigated the corrosion and carburizing behaviors of three Ni-based alloys (Incoloy 800 H T, Inconel 600, and Inconel 690) and discovered that they exhibited high corrosion resistance due to the formation of a thin and continuous chromium oxide layer (Cr_2O_3). Olivares et al. [43] conducted corrosion experiments on austenitic steel SS316 and nickel-based alloy Hastelloy-C276. Although these two materials have similar chromium contents, austenitic steel SS316 is susceptible to breakaway corrosion, whereas the nickel-based alloy Hastelloy-C276 successfully resists breakaway corrosion and ensures the integrity of the protective scale. Although SS316 can form a protective chromium-rich oxide layer such as Hastelloy-C276, the austenitic-oxide film interface may experience greater growth stress and thermal stress, thus causing the oxide film to be more susceptible to cracking and shedding. Oleksak et al. [44] conducted corrosion resistance experiments on Inconel 617 under high temperature CO_2, and discovered that its surface offered good protection.

In addition, corrosion experiments using different alloys have been conducted, and differences in corrosion resistance of different types of alloys are analyzed and compared. Martensite heat-resistant steel T91, austenitic heat-resistant steel TP347HFG, and Inconel 617 were compared by corrosion experiments [45]. Based on chromium-depleted and carburized zones, the corrosion resistance of heat-resistant steels and alloys in *S*–CO_2 can be evaluated based on the corrosion degradation depth. Researchers have demonstrated by the above method that Inconel 617 offers the best corrosion resistance, followed by austenitic heat-resistant steel TP347HFG. Fig. 5 (a) and (b) show weight gain and corrosion kinetics respectively [45]. The weight gain of T91 was much higher than those of TP347HFG and Inconel 617; VM12 ferritic steel, Sanicro 25 austenitic steel and Inconel 617 were tested in comparative experiments [46], and the results showed that Inconel 617 offered better corrosion resistance. Some types of Ni-based alloys were tested to determine the effect of pressure on the corrosion behavior in an *S*–CO_2 environment, where the results showed that pressure minimally affected the oxidation behavior [47]. The British company Heatric manufactured highly efficient compact microchannel printed circuit heat exchangers using austenitic stainless steel (AL-6XN, 304 L, 316 L, etc.) and Inconel 617 as materials, and constructed a

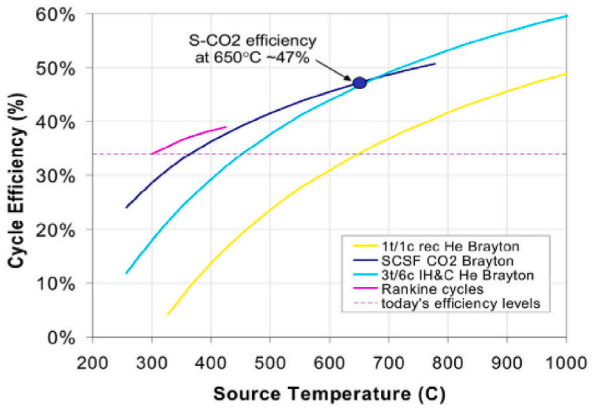

Fig. 2. Cycle thermal efficiency as a function of heat source temperature [14].

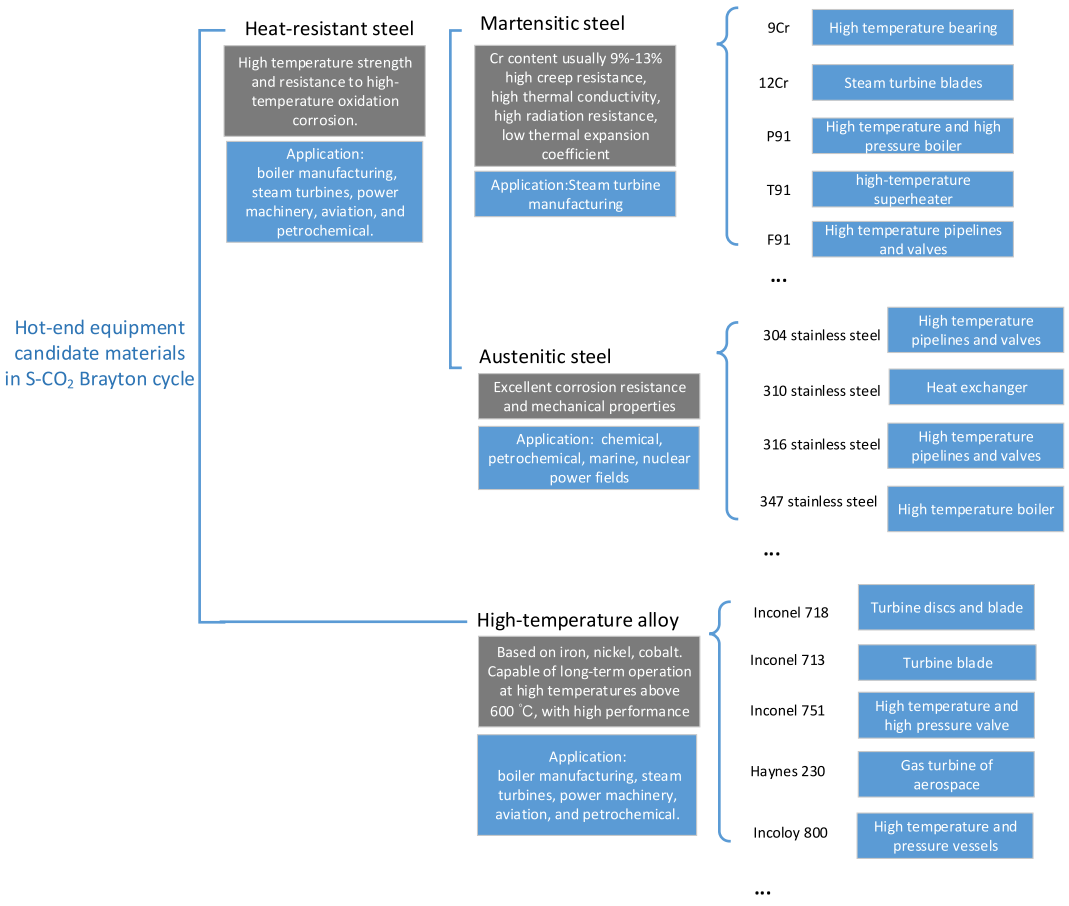

Fig. 3. Candidate materials used in *S*–CO_2 Brayton cycle and their characteristics.

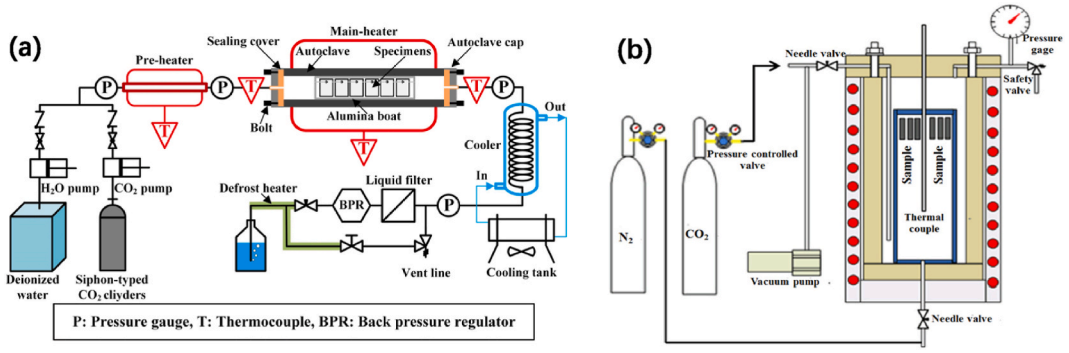

Fig. 4. Corrosion systems in high-temperature *S*–CO_2 Brayton cycle from (a) Gui et al. [39] and (b) Zhu et al. [40].

supercritical CO_2 split-flow recompression Brayton cycle unit at Sandia National Laboratory, which is already operational. Several experiments have been conducted on experimental devices, thus providing considerable experience and data for subsequent research [48]. The Massachusetts Institute of Technology and Tokyo Institute of Technology focused on austenitic stainless steels 304 and 316 for the design of heat exchanger materials in *S*–CO_2 cycle power generation systems [49,50].

To analyze the alloy corrosion behavior of key equipment in the *S*–CO_2 Brayton cycle system, researchers have primarily focused on martensitic steel (e.g., 9Cr-steel, 12Cr-steel, T91, and VM12), austenitic steel (e.g., 316FR, Sanicro, 25, Super 304H, and TP347HFG) and nickel-based superalloys (e.g., Inconel 600, Inconel 617, 690, and Incoloy 800 H T). These materials were used to conduct related experiments and investigate the corrosion behavior of alloys from the aspects of oxidation and carburization.

Table 1 and Table 2 lists the studies performed to analyze the corrosion behavior of different materials under different pressures,

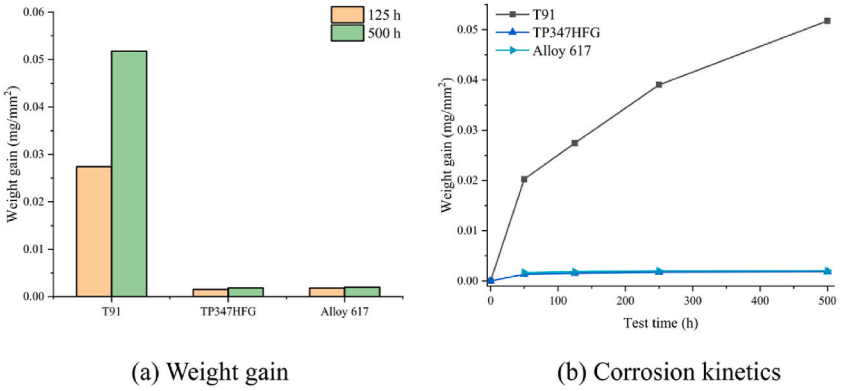

Fig. 5. (A) Weight gain and (b) corrosion kinetics of three types of investigated materials [45].

temperatures, impurities, and stress factors in recent years. Fig. 6 shows the most investigated alloys listed in Tables 1 and 2. As shown in Fig. 6, researchers selected different alloys for testing, including martensitic alloys, austenitic alloys, and high-temperature nickel-based alloys to select the material that performs the best in the *S*–CO_2 Brayton power cycle system. The alloys in the figure are considered to be more promising materials and thus have received significant attention. Inconel 625 is the most widely studied material.

2.2. Oxidation corrosion behavior of alloys

The oxidation of alloys refers to the phenomenon in which metal atoms lose electrons and react with the medium to form an oxide film, which damages the surface of the alloy. During long-term oxidation, the initially formed oxide film serves as protection. However, when the oxide film breaks and peels off, the internal alloy experiences continuous damage. Therefore, the formation and removal of oxide films are closely related to alloy corrosion.

The elemental content of an alloy significantly affects the formation of oxide films. In the 1970s, researchers [40,90–92] proposed the "available space theory" for the corrosion of 9%–12 % Cr steel in CO_2. This model describes the double-layer oxide film formation process. Fe diffuses into the outer layer and reacts with CO_2 to form an outer oxide film. This diffusion causes vacancies to appear between the oxide film and substrate, thereby providing vacancies for the internal reaction of Fe and Cr with CO_2. Simultaneously, pores are generated during the growth of magnetite to enable CO_2 to flow to the vacancies between the oxide film and substrate, thus providing CO_2 for internal reactions. The reaction is shown in Eqs. (1) and (2) [40]:

$$3Fe+4CO_2 \rightarrow Fe_3O_4+4CO \quad (1)$$

$$Fe+2Cr+4CO_2 \rightarrow FeCr_2O_4+4CO \quad (2)$$

Rouillard et al. [54] selected T91 steel (9 % Cr) to conduct relevant experimental analysis, and proposed a model in which voids promotes the growth of double-layer oxide films comprising magnetite and Fe_3-xCr_xO_4. Here, the value of x depends on the void depth in the oxide film. When the void depth reaches its maximum, the value of x reaches its maximum and $FeCr_2O_4$ is generated. Some researchers [39,41,93] have investigated and summarized the oxidation corrosion of metal materials, and concluded that the square of the weight gain or the thickness of the alloy oxide film is proportional to the oxidation time t, thus demonstrating a parabolic oxidation law.

The presence of Cr in alloys is beneficial for the formation of corrosion-resistant oxide films. The dense Cr_2O_3 oxide film can protect internal metals under high-temperature and high-pressure. T91 and 316, which are currently widely used in ultra-supercritical thermal power units and advanced carbon dioxide gas-cooled reactors, were selected to conduct corrosion tests (500 °C and 600 °C; 20 MPa) [68]. The results showed that the corrosion product of 316 was mainly a thin and dense layer of Cr_2O_3, while the corrosion product of T91 was mainly composed of outer columnar Fe_3O_4 and inner columnar Fe–Cr spinel. The corrosion products of T91 exhibited a porous structure and were not protected against further corrosion. This is because the chromium content of 316 was higher, which provided sufficient chromium to ensure the continuous growth of Cr_2O_3 during the corrosion process, and the affinity of chromium for oxygen was greater than that for iron. Cr_2O_3 grows at a sufficiently low rate in a high-temperature and high-pressure *S*–CO_2 environment, and only a small portion of the alloy is corroded. This protects the internal metal from oxidation, thereby affording high-temperature and high-pressure corrosion resistance.

When Ni-based alloys are corroded, other oxide films may form. Austenite AL-6XN and nickel-based alloy Haynes 230, which feature similar chromium contents, were subjected to corrosion experiments [57]. Haynes 230 exhibited less corrosion weight gain and fewer cracks on the surface of the oxide film, mainly because the protective layer of the nickel-based alloy contained a mixture of Cr_2O_3 and $NiCr_2O_4$. Pure Ni and Ni-x%Cr (x = 7, 14, 22, and 27) binary alloys were experimentally analyzed, and the results showed that a thicker NiO layer formed on the surface of pure Ni [94]. The Ni–7%Cr formed an oxide film composed of irregular Cr_2O_3 and NiO under the NiO surface layer. When the Cr content exceeded 14 %, a continuous Cr_2O_3 layer was generated, and the weight gain and oxide film

Table 1
Studies regarding corrosion of alloy in S–CO_2 at temperature of 400 °C–750 °C.

Reference	Materials	Temperature, Pressure and Duration	Notes
Gibbs et al. 2010 [51]	F91, HCM12A, 316SS, 310SS, AL-6XN, 800H, Haynes230, Alloy 625, PE-16, PM2000	20 MPa 610 °C 3000 h	HCM12A and F91 gain more weight than other alloys.
Furukawa et al. 2010 [52]	12Cr, 316 F R	20 MPa 400–600 °C 1991 h	No effect of pressure on corrosion observed.
Furukawa et al. 2011 [41]	9Cr, 12Cr, 316 F R	20 MPa 400–600 °C 8000 h	Follow the parabolic law. Weight gain of 316 F R is lower than martensitic steel.
Tan et al. 2011 [53]	Alloy 800H, AL-6XN, F91, HCM12A	20.7 MPa 650 °C 3000 h	Oxidation resistance of 800H alloy is better than that of AL-6XN alloy. Corrosion resistance of FM steel is worse than that of austenitic steel.
Rouillard et al. 2011 [54]	K90901(F91), S31603 (316 L), S30815, N08800 (800)	25 MPa 550 °C 310 h	Austenitic alloys 316 L, S30815 and 800 are much more resistant to corrosion than 9 wt% Cr, FM steel and T91.
Rouillard et al. 2012 [55]	T91	0.1/25 MPa 550 °C 1/322/1000 h	A growth model of void-promoted double layer oxide films is proposed.
Cao et al. 2012 [56]	SS310, SS316, Alloy 800H	20 MPa 650 °C 3000 h	Corrosion resistance: 800H > 310 S S > 316 S S
Firouzdor et al. 2013 [57]	AL-6XN, PE-16, Haynes230, Alloy 625	20 MPa 650 °C 500/1000/3000 h	Corrosion resistance of PE-16 alloy is better than that of SS316, which has higher chromium content. Al and Ti maybe play a role.
Lee et al. 2015 [42]	Alloy 800 H T, Alloy 690, Alloy 600	20 MPa 550–650 °C 1000 h	Carburizing resistance is impacted by the elements of matrix. Ni-based is better than Fe-based.
Furukawa et al. 2015 [58]	12Cr steel, T91	20 MPa 400–600 °C 5000/8000 h	The thickness of each oxide layer has a good proportional relationship with the weight gain.
Holcomb et al. 2016 [47]	Alloy 347H, Alloy 282, Alloy 625,	20.7 MPa 730 °C 500 h	Pressure has little effect on oxidation of nickel-based alloys.
Lee et al. 2016 [59]	Alloy 600, Alloy 690, Alloy 800 H T	0.1/10/20 MPa 550–650 °C 1000 h	Increasing the pressure would lead to more amorphous C at the oxide film or alloy interface.
Rouillard et al. 2016 [60]	9Cr, 12Cr	25 MPa 500–600 °C 8000 h	Increasing the pressure would accelerate the rate of carburizing corrosion.
Pint et al. 2017 [61]	Grade91, *E*-Brite, 347HFG, 310HCBN, APMT, Alloy 625, Alloy 230, CCA617	30 MPa 750 °C 500 h	Pressure had minimal effect on mass change and product.
Liang et al. 2018 [62]	T24, T91, Super304H, Haynes 282	0.1 MPa 600 °C 1000 h	Super 304H and Haynes 282 exhibit excellent corrosion resistance due to their higher Cr and Ni content.
Kim et al. 2018 [63]	316 L N (Al single layer), 316 L N (NiAl bi-layer)	20 MPa 650 °C 500 h	The weight gain of surface-modified 316 L N is less than that of ordinary 316 L N alloy.
Lee et al. 2018 [64]	Alloy 600 (diffusion-bond), Alloy 182 (fusion-weld)	20 MPa 550 °C, 650 °C 1000 h	The weight gain of alloy 182 fusion welding is about 3 times that of alloy 600.
Liang et al. 2019 [45]	T91, TP347HFG, Alloy 617	15 MPa 650 °C 500 h	T91 gained significantly higher weight than TP347HFG and 617 at 650 °C.

(*continued on next page*)

Table 1 (*continued*)

Reference	Materials	Temperature, Pressure and Duration	Notes
Gui et al. 2019 [39]	T91, VM12, Super304H, Sanicro25	15 MPa 650 °C 1000 h	For several tested alloys, the corrosion resistance is positively related to the chromium content.
Chen et al. 2019 [65]	AISI 430, AISI 630, AISI 347H, AISI 316 L N	20 MPa 650 °C 500 h, 1000 h	347H and 316 L N form a thick double oxide layer, the weight gain is much larger than others.
Gui et al. 2020 [46]	VM12, Sanicro25, Inconel 617	15 MPa 600 °C 1000 h	VM12 gained significantly more weight than Sanicro 25 and Inconel 617.
Brittan et al. 2020 [66]	Grade 92	20 MPa 450 °C, 550 °C 1000 h	Carburizing corrosion will become more serious with increasing temperature.
Bidabadi et al. 2020 [67]	F91	0.1,5,10 MPa 550 °C 500 h	In the range of 5–10 MPa, pressure has little effect on weight gain.
Yang et al. 2021 [68]	T91, SS316	20 MPa 500 °C, 600 °C 1000 h	Compared with 316 steel, the corrosion products of T91 have no further protective effect on corrosion.
Brittan et al. 2021 [69]	316 L, 316H	20 MPa 550 °C, 750 °C 1000 h	The oxide thickness at 750 °C is about 10 times that at 550 °C; Elevated temperature causes loss of plasticity.

thickness reduced significantly. The specific reaction is shown in Eq. (3):

$$xM + yCO_2 \rightarrow M_xO_y + yCO \tag{3}$$

In this equation, if M represents nickel, then x and y = 1; if M represents chromium, then x = 2 and y = 3.

In addition to Cr and Ni, other elements in the alloy, such as Al and Ti, affect the corrosion behavior. PE-16 showed better corrosion resistance than alloys with higher Cr contents, such as 316 stainless steel [57], which is attributable to the aluminum and titanium contained in it. Moreover, the Al-rich oxide film exhibited good adhesion to the alloy because of its thinness; therefore, even in the area where the Cr-rich oxide film was broken, a thin Al_2O_3 protective layer remained.

Although some experimental results [45,51,53] verified that the corrosion resistance of austenite is better than that of martensite, the chromium content in austenite selected by scholars is significantly larger than that of martensite, which may contribute to the results derived in these experiments. Chen et al. [65] selected alloy materials with similar chromium content to conduct experiments, and the results showed that the corrosion resistance of austenite may be weaker than that of martensite with a similar chromium contents. Fig. 7 [65] shows the weight gain of four alloys with similar Cr contents, where 430 is martensitic steel, 630 is ferritic steel, and 347H and 316 L N are austenitic steels. The corrosion resistance of the austenitic steel was favorable in the first 500 h; however, the weight gain increased significantly in the final 500 h and significantly exceeded that of the martensitic steel. The surface SEM images of the four alloys after 500 h (Fig. 8(a–d) [65]) show that the surface of the austenitic steel was severely cracked and tended to collapse.

The effect of the austenite and martensite microstructure on oxide film exfoliation can be summarized as follows: First, Cr has a large diffusion coefficient in martensite; therefore, sufficient Cr exists to form a Cr-rich protective layer when the oxide film is broken. Second, the growth stress at the interface between the austenite base layer and oxide film may be high, which renders the oxide film susceptible to cracking and collapsing. Finally, austenite has a large coefficient of thermal expansion, which results in a high thermal stress, thus causing the oxide film to crack and collapse [65].

In addition to Cr, Ni, and Al, some other alloying elements can also affect the corrosion behavior of alloys in *S*–CO_2. The effects of Ti and Nb on the oxidation behavior of Inconel 740H in high-temperature and high-pressure *S*–CO_2 environments (650–750 °C, 25 MPa) were discussed [95]. Ti and Nb may form oxide nodules on the surface, which will accelerate the oxidation of the matrix. Among them, the accelerated diffusion of Ti at high temperatures may lead to the enrichment of oxides. Loose Ti oxides are more prone to detachment. The oxide Nb_2O_5 of Nb will form growth stress on the metal, leading to the rupture of the Cr_2O_3 oxide layer and accelerating the peeling of Cr_2O_3. Therefore, both Ti and Nb have a negative impact on the corrosion performance of alloy Inconel740H In summary, in a high-temperature and high-pressure *S*–CO_2 environment, alloys containing Cr, Ni, and Al form a relatively stable oxide film, which demonstrates their high corrosion resistance. Due to the significant potential applications of these alloys in high-temperature *S*–CO_2 Brayton cycles, researchers must consider the possible corrosion behavior of these alloys over extended periods of use. Therefore, in order to mitigate or even prevent corrosion and alloy oxide spalling mechanisms, a clear and in-depth investigation into the mechanisms behind alloy oxide spalling mechanisms is essential. In addition, the corrosion behavior of steels with similar chromium contents but different microstructures are rarely investigated. Hence, further research regarding this topic is necessitated.

Table 2
Corrosion studies of alloy in supercritical CO_2 with impurities or stress.

Reference	Materials	Temperature, Pressure and Duration	Impurity or Stress	Notes
Huenert et al. 2011 [70]	13CrMo44, T24, *X*20CrMoV12-1, Alloy B, DMV 310 N, T92	0.1 MPa /3 MPa 500–700 °C 250 h, 1000 h	30%H_2O, 69%CO_2, 1%O_2/ 30%H_2O, 70%CO_2	The increase of pressure of corrosive gases speed up the carburization kinetics and oxidation kinetics.
Mahaffey et al. 2014 [71]	SS347, 800H, AFA	2900 psi 550 °C, 650 °C 1000 h	99.999%CO_2/99.95%CO_2	Research-grade CO_2 has greater weight gain compared to industrial-grade CO_2.
Nguyen et al. 2015 [72]	Model alloys, Fe–9Cr, Fe–20Cr, Fe–20Cr–20Ni with 0.1 % Ce or 2 % Mn	0.1 MPa 650 °C 1000 h	Ar–20%CO_2/Ar–20% CO_2–20%H_2O	Water vapor significantly reduces the oxygen absorption rate and chromia scaling rate of Fe–20Cr–20Ni.
Nguyen et al. 2015 [73]	Fe–20Cr Fe–20Cr–20Ni With Si (0.1,0.2,0.5 wt%)	0.1 MPa 818 °C 240 h	Ar–20%CO_2- 20%H_2O	Fe–20Cr alloy fails to form protective Cr_2O_3 scale in wet CO_2.
Mahaffey et al. 2016 [74]	Haynes230	20 MPa 650 °C, 750 °C 1000 h	10 ppm O_2/ 100ppmO_2	Oxygen impurities significantly enhanced oxidative corrosion of the material and oxide exfoliation was observed.
Mahaffey et al. 2018 [75]	Alloy 625	20 MPa 750 °C 1000 h	Research-grade RG+100ppmO_2/RG+1pctCO	Both O_2 and CO impurities increase the weight gain of alloy.
Pint et al. 2018 [76]	Alloy 625	0.1 MPa, 30 MPa 750 °C 5000 h	CO_2(0.1 MPa,30 MPa)/ Air (0.1 MPa)	The oxide scale formed in Alloy 625 in s-CO_2 at 30 MPa is thicker and the grain size of Cr_2O_3 is smaller than in air.
Olivares et al. 2018 [77]	Alloy 282, Alloy 230[b], HR160, HR120, Alloy 188[a]	20 MPa,1 atm 700–1000 °C 1000 h	CO_2(20 MPa), Air (1 atm)	Several high-nickel chromia-forming alloys behaved protectively in CO_2 and air, forming scales containing principally a layer of Cr_2O_3.
Oleksak et al. 2018 [78]	Grade 22, Grade 91, 347H, 310 S, Alloy 282, Alloy 740H, Alloy 617, Alloy 625, Alloy 230	0.1/20 MPa 550–750 °C 1500–2500 h	CO_2/95%CO_2, 4%H_2O,1%O2/95%CO_2, 4% H_2O,1%O2, 0.1%SO2/Air/	Effect of pressure on oxidation is small. The addition of SO_2 significantly enhanced the rate for austenitic Fe alloys.
Oleksak et al. 2019 [79]	Alloy 625, Alloy 600, Alloy 745, Alloy 230, Alloy 263, Alloy 282	0.1 MPa, 750 °C 2500 h	95%CO_2–4%H_2O–1%O_2	Several nickel alloys form protective oxide layers under the set impurity conditions.
Pint et al. 2019 [80]	304H, 25SS, 310HCbN, Alloy 625, 230, 617 B, 282 (heat 1,2), Super Alloy 247	30 MPa, 750 °C 2500 h	Research grade CO_2/ Industrial grade CO_2/ CO_2+1%O_2+ 0.25%H_2O	For alloys in impurity-containing environment, the increase in pressure results in a thicker reaction product.
Gui et al. 2019 [81]	T91	15 MPa 600°C–650 °C 1000 h	Stress	Stress increases the corrosion rate of T91.
Lehmusto et al. 2020 [82]	Alloy 316, Alloy 120, Alloy 625, Alloy 740,	20 MPa 700 °C 1500 h	Air (not quantitative)	Corrosion is exacerbated by the entry of impurity air, especially 316 and 120.
Xie et al. 2020 [83]	Model alloys Ni-(20, 30) Cr with (0,1,5,15 %) Fe	0.1 MPa 800 °C 500 h	Ar–20%CO_2- 20%H_2O	Corrosion in wet CO_2 avoids scale peeling.
Oleksak et al. 2020 [84]	304H, 347H, 310 S, *E*-Brite Grade 22 Grade91	0.1 MPa 550 °C 2500 h	95%CO_2,4 % H_2O, 1 % O_2, (0.1%SO_2)	The addition of SO_2 has little effect on low-chromium steels, but enhances the corrosion of high-chromium steels.
Kim et al. 2020 [85]	Ni–16Cr–9Fe	0.1/20 MPa 650 °C 700 h	Stress Air/CO_2/ *S*–CO_2	Creep rupture life of alloys in *S*–CO_2 is shorter compared to air and CO_2 environments.
Akanda et al. 2020 [86]	P91	0.1 MPa 650 °C 1000 h	Stress thickness: 0.5 mm, 2.54 mm	Alloy thickness has a large effect on mechanical properties, the mechanical properties of thinner P91 are severely degraded by exposure.

(*continued on next page*)

Table 2 (*continued*)

Reference	Materials	Temperature, Pressure and Duration	Impurity or Stress	Notes
Li et al. 2021 [87]	SS310 Alloy 740	30 MPa 600 °C 1000 h	100 ppm H_2O /100 ppm O_2	Addition of H_2O impurity significantly enhanced the oxidation, while the presence of O_2 led to the opposite trend
Rozman et al. 2021 [88]	MARBN-type9Cr	0.1 MPa 650 °C	Stress Air/CO_2	Carbides forming beneath growing oxides promote environmentally-assisted cracking, accelerating failure in CO_2.
Pei et al. 2021 [89]	Nickel-based single crystal superalloy	0.1 MPa 1000 °C, 105 °C 600 h	Stress: 40 MPa, 60 MPa, 120 MPa	The external tensile stress did not change the layered structure of the alloy oxide layer, but increased the oxidation rate of the alloy.

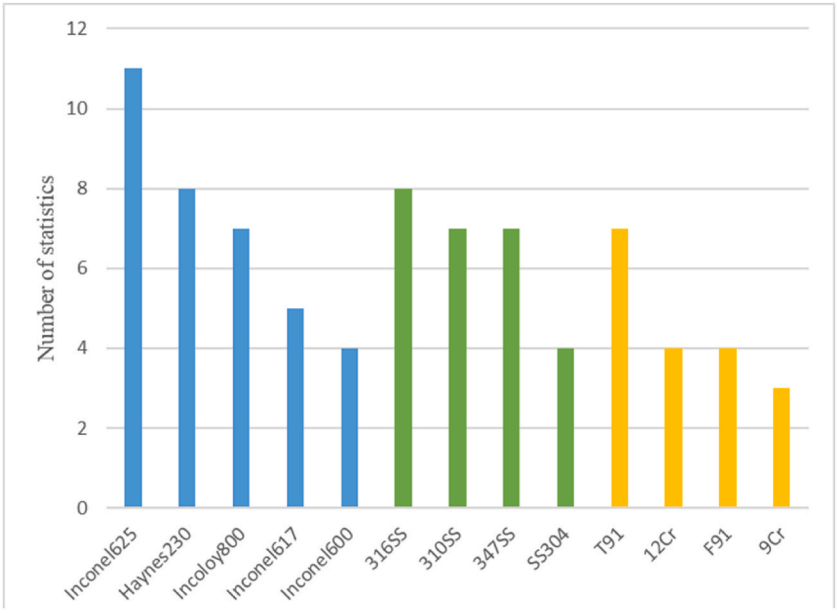

Fig. 6. Statistics of alloys studied in the corrosion experiments (blue for nickel-based alloys, green for austenitic stainless steels, and yellow for martensitic stainless).

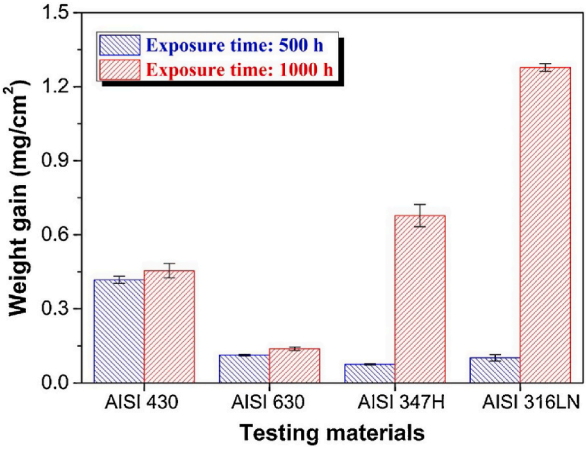

Fig. 7. Weight gain of four types of steel after 500 h and 1000 h [65].

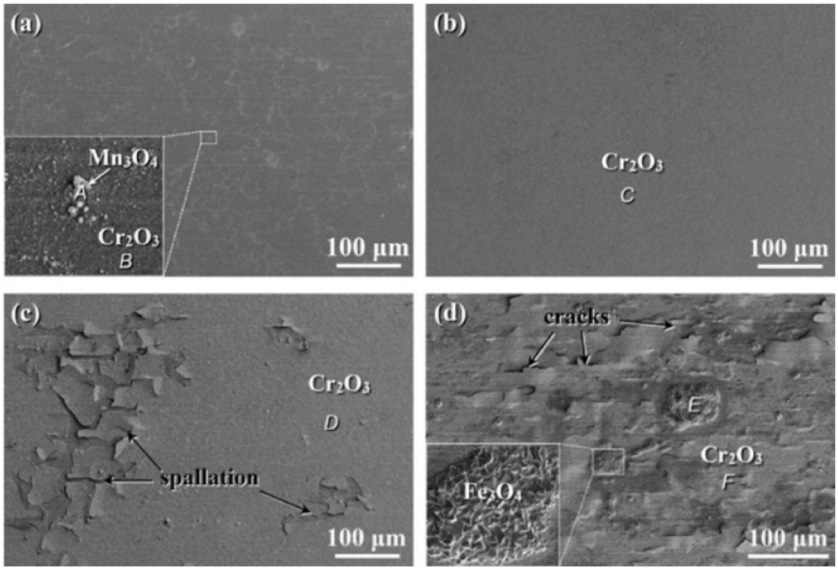

Fig. 8. Surface microstructure of four steels after 500 h (a)430; (b)630; (c)347H; (d)316 L N [65].

2.3. Carburization corrosion of alloys

Carburization refers to the infiltration of carbon atoms into an alloy, and significantly affects various steel and superalloys. Vamshi et al. [96] reported that carburization affects the creep-resistance of steel and reduces its oxidation resistance. In addition, carburization reduces the ductility of alloys and increases the difficulty of welding. Compared with the steam Rankine cycle and helium Brayton cycle, carburizing corrosion is a unique corrosion behavior when *S*–CO_2 is used as the working fluid in the Brayton cycle. Scholars have begun to focus on to the effects of temperature, pressure, impurities and other factors on carburization. An *S*–CO_2 environment may exacerbate carburization. Previously, the effect of carburizing in *S*–CO_2 environments at 750 °C and 550 °C was compared with that in 316 S S [69]; the result showed that carburizing did not result in ductility loss at 550 °C, whereas it resulted in significant ductility loss to the alloy at 750 °C. Incoloy 800 H T exposed to *S*–CO_2 was subjected to corrosion experiments and compared to samples exposed to vacuum and air [97]. Additionally, researchers observed a carbon-accumulated layer at the oxide-matrix interface. Subsurface carbide precipitation occurred in all samples but was more pronounced in the *S*–CO_2 exposed specimen, thus indicating that carbon diffused inward from the carbon-accumulated layer at the oxidation-matrix interface. Nickel-based alloys generally exhibit stronger carburizing resistance than austenitic alloys. Inconel 740 exhibited better resistance to carburization than SS310. Fig. 9 [56] shows the carbon deposition on the oxide film surface, including plan view (Fig. 9 (a)), FIB cross section view (Fig. 9 (b)) and EDS line scan (Fig. 9 (c)) analysis. Based on cross-sectional EDS analysis, the deposited film was determined to be pure carbon, which can penetrate the alloy through the grain boundary diffusion of gas molecules [30].

Moreover, carburization occurred under the oxide film. Lee et al. [42] summarized the carburizing process of un oxide film as follows.

First, when CO_2 passes through the oxide film, it reacts with metal M to generate CO. The reaction is shown in Eq. (4).

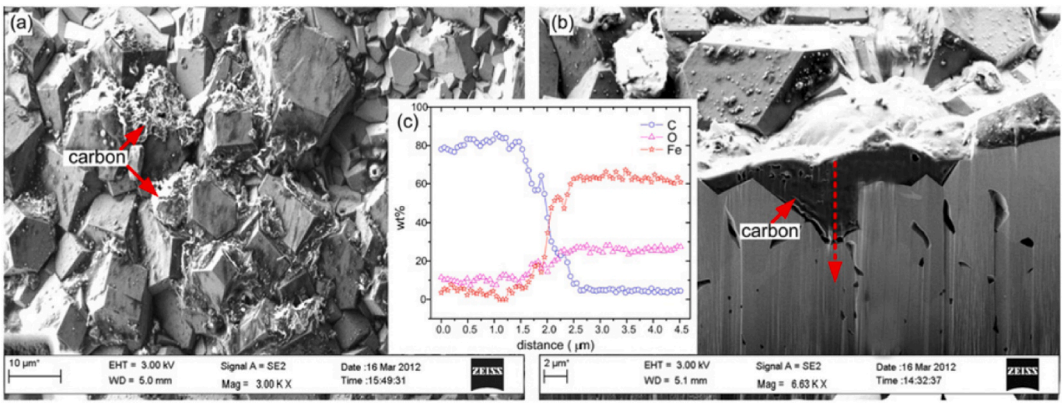

Fig. 9. Deposition of carbon flakes on surface of oxide scale (a) plan view; (b) FIB cross section view; (c) EDS line scan analysis [56].

$$xM + yCO_2 \rightarrow M_xO_y + yCO \quad (4)$$

In the formula above, M can be Fe or Cr.
Subsequently, carbon is formed via the Boudouard reaction in Eq. (5) [55].

$$2CO \rightarrow C + CO_2 \quad (5)$$

In addition, Eqs. (6) and (7) contribute to carbon deposition during corrosion [55]:

$$xM + yCO_2 \rightarrow M_xO_{2y} + yC \quad (6)$$

where, M can be Fe, Cr or Mn; and

$$xM + yCO \rightarrow M_xO_y + yC \quad (7)$$

where, M can be Fe or Cr.

Different oxide films exhibit different protective effects against carburizing corrosion. Although Cr_2O_3 can effectively resist oxidation corrosion, it is not a perfect protective layer against carburization corrosion because CO and CO_2 can pass through the Cr_2O_3 layer through nanochannels and cracks, and carburizing corrosion occurs after a series of reactions [98]. Surface treatments can improve the carburization resistance of Ni-based alloys [99]. Inconel 600 was processed using Al deposition and high-energy electron beam. Investigations into the corrosion resistance of Inconel 600 showed that the transition Al_2O_3 generated at 600 °C did not exhibit sufficient anti-carburization properties, whereas α-Al_2O_3 pre-oxidized at 900 °C partially inhibited the inward diffusion of C, CO and CO_2, thus demonstrating excellent carburization resistance. In addition, the carburization resistances of the different base alloys differed significantly. Iron-based Incoloy 800 H T exhibited a large carburized area after the corrosion test, and chromium-rich carbide $M_{23}C_6$ was observed in the amorphous carbon layer; meanwhile, nickel-based alloys 600 and 690 did not possess large carburized areas and carbides. Lee et al. believed that this result was due to the lower Cr activity, lower carbon solubility and lower diffusivity in nickel-based alloys.

According to Cao et al. [56], during corrosion process, the free carbon trapped in the internal oxide film increases the porosity and results in the spallation of the oxide film. Similar conclusions were presented by Furukawa et al. [41], who argued that carburization contributed to the cracking and peeling of the oxide film, which aggravated the corrosion behavior of the alloy.

Currently, studies regarding carburization are scarce. Because carburization involves diffusion on the surface of an oxide film and a series of reactions in the lower layer of the oxide film, more experiments are required to investigate the effects of these various factors.

3. Effect of external environment on corrosion behavior of alloys

3.1. Temperature

At lower temperatures (less than 400 °C), the chemical properties of CO_2 are generally believed to be stable and the corrosion rate is extremely slow. Zhang et al. [100] reported low the corrosion rates of stainless steel 13Cr of only 0.3–0.8 mm/a at 50 °C, 80 °C, 110 °C and 130 °C. However, as the temperature increased, the molecules gained more energy and collided with each other more intensely, which can result in an energy level exceeding the activation energy and thus higher corrosion rates [101]. Moreover, different corrosion products may be generated at higher temperatures [102].

At the typical temperature of the *S*–CO_2 Brayton cycle, the thickness and composition of the oxide layer may change as temperature increases. Two ferritic-martensitic steels (12Cr steel and T91) were exposed to 400 °C–600 °C, and metallurgical analysis was

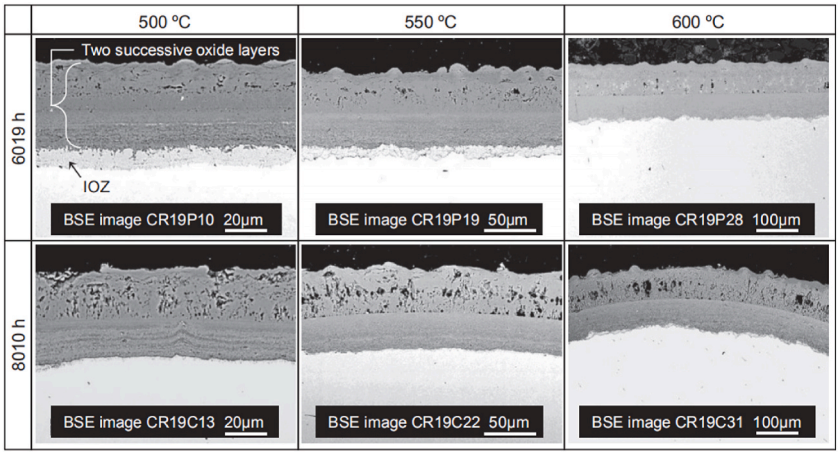

Fig. 10. SEM images of cross-section of 12Cr-steel at 20 MPa in *SC*-CO_2 [58].

conducted. It was discovered that the thickness of each oxide layer increased with exposure time due to parabolic oxide growth [58]. Moreover, as shown in Fig. 10 [58], the 600 °C sample corroded more severely than the 550 °C sample, and the thickness of the oxide layer increased with temperature.

In the high-temperature environment of the Brayton cycle, CO_2 gas is more corrosive than dry oxygen. Ni-(5, 10, 20, 25, and 30 wt %) Cr was subjected to corrosion experiments in Ar–20CO_2 and Ar–20O_2 atmospheres in a previous study [103]. The result showed that all alloys underwent breakaway oxidation in CO_2, thus resulting in a nickel-rich oxide layer on the outside and other oxides on the inside. A higher scaling rate in CO_2 compared with that in oxygen requires higher alloy chromium concentrations to sustain the Cr_2O_3 scale growth. Based on predictions, 25 % Cr in oxygen is sufficient, whereas 30 % Cr in carbon dioxide is insufficient. The model alloy Ni-(5, 10, 20, 25, 30 wt%) Cr was subjected to corrosion tests at different temperatures [104]. The result showed that elevated temperatures accelerated the oxidation kinetics of low chromium alloys, but significantly reduced the oxidation rate of high-chromium alloys by promoting the formation of chromia bands or scales. The critical chromium concentration required for the formation and maintenance of chromium scales decreased as temperatures, which is in accordance with diffusion theory. Not only that, the study by Brittan et al. [66] showed that an increase in temperature resulted in more severe corrosion based on both mass and image analyses. Fig. 11 [66] shows the cross-section of the samples obtained via SEM, which indicates that the average oxide thickness of P92 was 11.7 ± 1.7 μm at 450 °C (Fig. 11 (a, b)) and 36.9 ± 2.8 μm at 550 °C (Fig. 11 (c, d)). However, the carburization analysis showed that more carbon was deposited at 550 °C and that the carburization depth at 450 °C was approximately twice that at 550 °C.

In summary, the corrosion resistances of different alloys in an *S*–CO_2 environment at different temperatures are different. Therefore, corrosion experiments for different temperature sections are essential to understand the operating temperature ranges of various alloys and to select suitable alloys to manufacture different equipment (such as heat exchangers and turbines). Thus, economic optimization can be achieved to ensure safety and efficiency.

3.2. Impurities

In actual operating systems, *S*–CO_2 contains impurities (H_2O, O_2, CO, and sulfur-containing gases). Generally speaking, impurities in the *S*–CO_2 Brayton power cycle system are caused by the impure CO_2 working fluid itself and impurities generated by system leakage. The purity of industrial grade CO_2 can reach 99.95 %. The source of CO_2 may be the oxygen rich combustion of coal, which may lead to the generation of CO and sulfur containing gas impurities. On the other hand, leaks can cause the air to enter, bringing in oxygen impurities and water vapor impurities. In order to reduce the generation of these impurities, the sealing of the system can be improved and the source of CO_2 should be optimized. The type and content of these impurities are closely related to the corrosion behavior. An analysis of the effect of these impurities on the corrosion behavior facilitates CO_2 monitoring to reduce equipment corrosion.

Air impurities can reduce the corrosion resistance of alloys. Alloys 316, 120, 625, and 740 were exposed to 20 MPa research grade CO_2 at 700 °C for up to 1500 h [82]. The result showed that the group with leaked air exhibited more significant corrosion than the others. The increased severity of corrosion manifested in the forms of weight gain and a thicker oxide film of the alloy, particularly in alloys 316 and 120 with higher Fe content. Mahaffey et al. [71] investigated the corrosion behavior of several ferritic and martensitic steel exposed to industrial (99.95 %) and research-grade (99.999 %) CO_2, respectively, and discovered that the corrosion weight gain of the alloys in industrial grade CO_2 was similar to or lower than that in research grade CO_2. The effect of water vapor on the corrosion of alloys in *S*–CO_2 requires further research. Ni-(20, 30)Cr-(Fe) alloys were tested for their oxidation behavior in wet CO_2 at 800 °C [83]; during the wet CO_2 reaction, they were free from scale exfoliation, which allowed their mechanical integrity to b maintained. These results are attributed to water vapor. However, according to Nguyen et al. [73], the Fe–20Cr alloy cannot form and maintain a Cr_2O_3 protective layer in CO_2.containing water vapor.

The oxygen impurities increase the corrosion weight of the sample. Ni-based alloy Haynes 230 was investigated for their corrosion behavior in *S*–CO_2 at 650 °C and 750 °C [74], which is shown in Fig. 12(a) and (b). The results showed that in high-purity

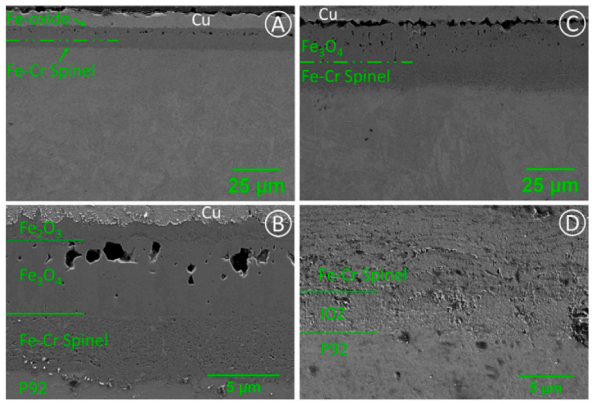

Fig. 11. Oxide of P92 exposed for 1000 h to CO_2 at 450 °C (a, b) and 550 °C (c, d) [66].

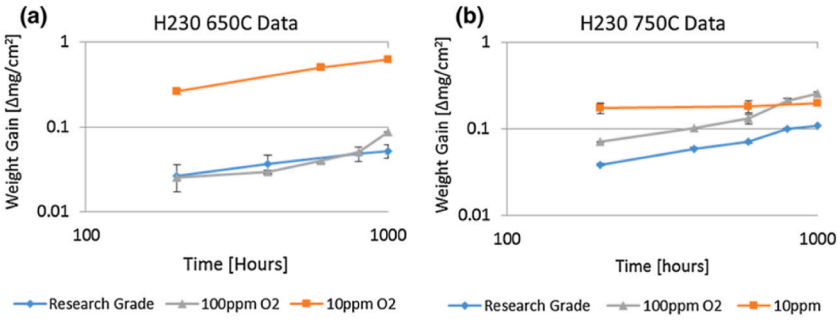

Fig. 12. Time-dependent weight gain data for alloy Haynes 230 at CO_2 purity levels (a) 650 °C and (b) 750 °C [74].

research-grade CO_2, the alloy exhibited good corrosion resistance via a thin and uniform protective oxide layer on the surface; however, after the introduction of 10 and 100 ppm oxygen impurities, oxidation corrosion significantly, thus resulting in oxide spallation and nodule formation. Based on the weight gain trend in Fig. 12 [74], the addition of oxygen impurities increased the weight gain of the samples compared with the finding for the samples exposed to RG CO_2, as well as resulted in a larger standard deviation and a slight deviation from the parabolic growth behavior.

CO impurities may alter the corrosion products and oxide morphology. The corrosion behavior of alloy 625 was tested in three different *S*–CO_2 environments: experimental grade (RG, 99.999 % purity) CO_2, RG CO_2+0.01 % O2, and RG CO_2+1 % CO [75]. The corrosion weight gain results are shown in Fig. 13 [75]. The weight gain of the alloy in a pure CO_2 environment was the lowest, and the addition of O_2 and CO accelerated the corrosion of the alloy. Further analysis proved that the alloy surface in a pure CO_2 environment contained uniform Cr_2O_3. In an oxygen-containing environment, because the reaction rate of chromium is higher than its diffusion rate in the matrix, other metal elements are oxidized when chromium under the oxide film is depleted, thus resulting in the appearance of nickel and iron oxide films on the surface of the alloy. Although no oxide films of nickel and iron were observed on the surface of the alloy in the CO-containing environment, a duplex oxide containing carbon was generated. Moreover, the higher porosity and carbon deposition in the 1 pct CO-exposed samples increased cracking and generated more diffusion pathways which further enhanced the corrosion rate.

In recent years, the effects of sulfur-containing impurities, including SO_2 and H_2S, on the corrosion of high-temperature materials, have received significant attention. Several austenitic alloys, such as grade 22, 91, and 347H alloys, were subjected to corrosion experiments containing SO_2 impurities at high temperatures and pressures [78]. The result showed that SO_2 significantly increased the oxidation rate of austenitic ferroalloys. Additionally, the corrosion resistance of several other alloys were investigated [84], and results showed that SO_2 minimally affected low-chromium steels but exacerbated the corrosion of high-chromium steels. Moreover, the structures of the corrosion products might change. The corrosion of T91 in *S*–CO_2 containing 100 ppm SO_2 or H_2S impurities at 550 °C and 15 MPa were tested [105]. Both H2S and SO_2 impurities significantly exacerbated the corrosion of T91 and altered the structure of the corrosion products.

To date, studies regarding the effect of gas impurities on corrosion behavior under high temperature and pressure are few. In recent years, more experiments have been performed to investigate the corrosion behavior of alloys in *S*–CO_2 environments. However, most of the corrosion experiments focused on studying the effects of single gas impurities [105–107], whereas few corrosion experiments have been conducted to examine the effect of mixed gas impurities on alloys.

3.3. Pressure

In a pure *S*–CO_2 environment, pressure minimally affects the formation of the oxide films. Various studies have shown that in a

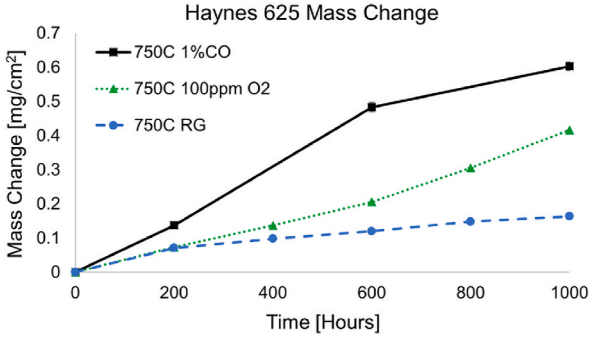

Fig. 13. Mass change data for 625 exposed to different CO_2environments at 750 °C, 20 MPa for 1000 h [75].

S–CO_2 environment, the corrosion rate of an alloy is less affected by pressure [47,52,61]. Fukukawa et al. [52] discovered that the corrosion rate of Ni-based alloys did not significantly change with pressure. Several iron-based and nickel-based alloys were subjected to corrosion experiments (750 °C, 200–300 bar), where the result showed that pressure exerted the least effect on mass change and product [61]. However, in a CO_2 environment with impurities, pressure significantly affected the role of impurities [80]. Increasing the partial pressure of the impurity changes its concentration, which may increase the corrosion rate [108]; In addition, an increase in pressure has been shown to alter the formation of corrosion products [109].

Pressure change significantly affects the carburization of martensitic steel. Based on experiments conducted on 9%-12%Cr martensitic steel from 0.1 to 20 MPa [60], one can conclude that pressure increase accelerates the rate of carburizing corrosion. Other studies pertaining to nickel-based alloys showed that an increase in pressure resulted in more amorphous C at the oxide film or alloy interface [59].

3.4. Stress

Stress, including tensile, bending, torsional, and thermal stresses, is typically encountered in powertrain components. In this context, the blades are subjected to a large centrifugal tensile stress during high-speed operation, and the root tooth supports the centrifugal force completely [110]. Alternating stress formed by tensile, bending, torsional, and exciting forces directly promoted the generation of surface cracks until the blade broke [111]. Stress corrosion cracking refers to the formation of cracks in alloys under the simultaneous effect of stress and corrosive media, which occurs typically in conventional and nuclear power steam turbines. Stress corrosion cracking refers to the formation of cracks in alloys under the simultaneous effect of stress and corrosive media, which occurs typically in conventional and nuclear power steam turbines.

Owing to the high temperature and high-pressure environment of *S*–CO_2, the alloy material undergoes creep. As early as the 1960s, scholars have investigated the creep behavior of alloys in high-temperature CO_2 environments. Domagala et al. [112] determined the properties of type 347 stainless steel, an Fe–Al–Cr alloy designated 261C, and a zirconium-base alloy in high-temperature CO_2. Many experiments have shown that the composition of environmental gases can affect the creep of alloys. The creep and stress rupture results of 304 stainless steel in wet and dry CO_2 and argon were compared [113]. The results indicated that the creep strength of 304 stainless steel in CO_2 was greater than that in argon gas. At a certain temperature, the strength of this effect increased with the temperature and decreased with stress. The minimum creep rate, elongation percentage, and rupture life were determined. A creep test was conducted on 9Cr martensitic steel at 650 °C and 0.1 MPa, and the results were directly compared with those of a creep test conducted in air [88]. The results showed that the carbides formed beneath the growing oxides can promote environmentally-assisted cracking, thus accelerating failure in CO_2. Fig. 14(a) and (b) [88] shows the cross-section of the scale of the specimen under both conditions respectively; as shown, the overall oxidative damage of the CO_2 creep test specimen occurred in a thicker layer than that of the specimen subjected to creep test in air. Ni–16Cr–9Fe subjected to the creep test in air, atmospheric CO_2 and *S*–CO_2 at 650 °C [85]. The results showed that the creep rupture life in *S*–CO_2 was shorter than those in air and CO_2 environments, and that the difference was greater at a lower stress. Moreover, the properties of Ti oxides may also affect the creep performance of the alloy. The Ti rich oxides produced in the experiment are prone to brittleness, which may accelerate the propagation of oxide layer cracks and lead to accelerated creep.

Corrosion experiments were conducted to test the effect of stress loading on the alloy. According to Gui et al. [81], under the same temperature and pressure conditions, the corrosion rate of a T91 tube under stress-loading was much higher than that under unstressed conditions. The corrosion products of the two samples were similar. The outer layer was a Fe-rich oxide and the inner layer was a Fe–Cr oxide. By contrast, a significant amount of carbide precipitation was observed in the Fe–Cr-rich corrosion layer of the stress-loaded samples. Currently, most stress corrosion experiments on alloys in *S*–CO_2 are conducted under non-high temperature conditions; therefore, stress corrosion in the Brayton cycle power generation system must be further investigated.

4. Conclusion

In this study, the corrosion behavior and characteristics of alloys in an *S*–CO_2 environment were reviewed, the results of recent corrosion experiments were summarized, and various factors affecting corrosion were analyzed. In summary, the conclusions obtained are as follows.

(1) Oxidative corrosion and carburization of alloys occurred simultaneously in the *S*–CO_2 Brayton cycle system. Currently, the corrosion behavior of martensitic steel (e.g., 9Cr-steel, 12Cr-steel, T91, and VM12), austenitic steel (e.g., 316FR, Sanicro 25, Super 304H, and TP347HFG) and nickel-based superalloys (e.g., alloys 600, 617, 690, and 800 H T) are prioritized. The corrosion resistance of austenitic steel appeared to be higher than that of martensite and was positively related to the chromium content. The corrosion resistance of superalloys appeared to be higher than those of ferritic, martensitic and austenitic steels; this is because superalloys can form a protective oxide layer more easily, thus preventing further corrosion.

(2) The square of the weight gain or thickness of the oxide film of the alloy was proportional to the oxidation time t, based on the law of parabolic oxidation. In high-temperature and high-pressure *S*–CO_2 environments, elements, such as Cr, Ni, and Al, were conducive to corrosion resistance. Nickel-based alloys exhibited stronger resistance to carburization than iron-based alloys. Carburization may cause the oxide film to peel off, thereby increasing corrosion.

(3) An increase in temperature significantly accelerated corrosion and caused high-chromium alloys to reduce the oxidation rate. O_2 significantly enhanced the oxidation corrosion of the alloys. H_2O inhibited the formation of oxide films and CO accelerated

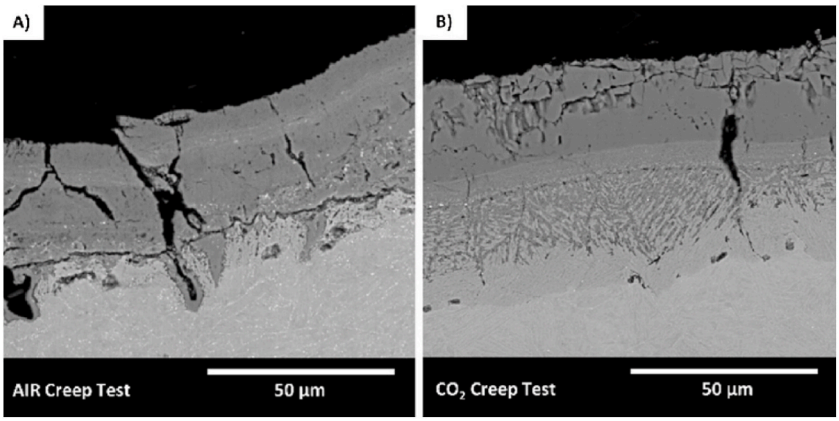

Fig. 14. Cross section of specimens showing oxide scale at 650 °C (a) Creep tested in air at 207 MPa and (b) creep tested in gaseous CO_2 at 207 MPa [88].

the rate of carburizing corrosion. The effect of pressure on corrosion in aS-CO_2 environment was negligible; however, the presence of impurities may enable the pressure to yield different effects.

In summary, more comprehensive studies should be conducted. First, an experimental study on the effects of the alloy structure and specific alloy elements on oxidation and carburization corrosion should be conducted to clarify the corrosion mechanism of the alloy under *S*–CO_2 Brayton cycle conditions. Second, the corrosion resistance of alloys in a flowing CO_2 environment and under stress loading should be investigated more comprehensively. In addition, more studies should be performed to investigate stress corrosion under *S*–CO_2 Brayton cycle conditions. Furthermore, the actual service time and operating conditions of the equipment as well as the actual operating conditions of the components, such as pressure and temperature, should be considered more comprehensively. Based on corrosion theory, the corresponding oxidation corrosion and carburizing models can be established, and the alloy corrosion simulation in the *S*–CO_2 Brayton cycle system must be investigated to predict the service life and safety of the equipment and the. Finally, because evaluation standards for materials are not available currently, a more comprehensive alloy corrosion evaluation system should be established for the *S*–CO_2 Brayton cycle to quantitatively assess the corrosion resistance of alloys.

Data availability statement

No data was used for the research described in the article.

CRediT authorship contribution statement

Ziyuan Xu: Writing – original draft, Writing – review & editing. **Yingying Yang:** Conceptualization, Funding acquisition, Methodology, Project administration, Supervision, Writing – review & editing. **M.A.O. Shijie:** Data curation, Formal analysis, Investigation, Methodology, Visualization. **Weidong Wu:** Conceptualization, Funding acquisition, Project administration, Supervision. **Qiguo Yang:** Conceptualization, Funding acquisition, Project administration, Supervision.

Declaration of competing interest

The authors declare that they have no known competing financial interests or personal relationships that could have appeared to influence the work reported in this paper.

Acknowledgements

This work was supported by the National Natural Science Foundation of China (No. 52006146) and the Capacity Building Project of Some Local Colleges and Universities of Shanghai Science and Technology Commission (No. 20060502000).

References

[1] W. Chu, K. Bennett, J. Cheng, Y. Chen, A review of supercritical CO2 Brayton cycle using in renewable energy applications, Renewable Energy Sustain. Dev. 4 (2018) 14–20, https://doi.org/10.21622/resd.2018.04.1.014.
[2] G.D. Pérez-Pichel, J.I. Linares, L.E. Herranz, B.Y. Moratilla, Potential application of Rankine and He-Brayton cycles to sodium fast reactors, Nucl. Eng. Des. 241 (2011) 2643–2652, https://doi.org/10.1016/j.nucengdes.2011.04.038.
[3] P. Schwarzbözl, R. Buck, C. Sugarmen, A. Ring, M.J. Marcos Crespo, P. Altwegg, J. Enrile, Solar gas turbine systems: design, cost and perspectives, Sol. Energy 80 (2006) 1231–1240, https://doi.org/10.1016/j.solener.2005.09.007.

[4] A. Yu, W. Su, X. Lin, N. Zhou, Recent trends of supercritical CO2 Brayton cycle: bibliometric analysis and research review, Nucl. Eng. Technol. 53 (2021) 699–714, https://doi.org/10.1016/j.net.2020.08.005.

[5] Y. Yang, Y. Huang, P. Jiang, Y. Zhu, Multi-objective optimization of combined cooling, heating, and power systems with supercritical CO2 recompression Brayton cycle, Appl. Energy 271 (2020), 115189, https://doi.org/10.1016/j.apenergy.2020.115189.

[6] F. Crespi, G. Gavagnin, D. Sánchez, G.S. Martínez, Supercritical carbon dioxide cycles for power generation: a review, Appl. Energy 195 (2017) 152–183, https://doi.org/10.1016/j.apenergy.2017.02.048.

[7] J. Sarkar, Thermodynamic analyses and optimization of a recompression N2O Brayton power cycle, Energy 35 (2010) 3422–3428, https://doi.org/10.1016/j.energy.2010.04.035.

[8] P. Wu, Y. Ma, C. Gao, W. Liu, J. Shan, Y. Huang, J. Wang, D. Zhang, X. Ran, A review of research and development of supercritical carbon dioxide Brayton cycle technology in nuclear engineering applications, Nucl. Eng. Des. 368 (2020), 110767, https://doi.org/10.1016/j.nucengdes.2020.110767.

[9] J. Xu, C. Liu, E. Sun, J. Xie, M. Li, Y. Yang, J. Liu, Perspective of S−CO2 power cycles, Energy 186 (2019), 115831, https://doi.org/10.1016/j.energy.2019.07.161.

[10] Y. Chen, P. Lundqvist, A. Johansson, P. Platell, A comparative study of the carbon dioxide transcritical power cycle compared with an organic rankine cycle with R123 as working fluid in waste heat recovery, Appl. Therm. Eng. 26 (2006) 2142–2147, https://doi.org/10.1016/j.applthermaleng.2006.04.009.

[11] J. Hu, W. Deng, Application of supercritical carbon dioxide for leather processing, J. Clean. Prod. 113 (2016) 931–946, https://doi.org/10.1016/j.jclepro.2015.10.104.

[12] Y. Liu, Y. Wang, D. Huang, Supercritical CO2 Brayton cycle: a state-of-the-art review, Energy 189 (2019), 115900, https://doi.org/10.1016/j.energy.2019.115900.

[13] A.D. Akbari, S.M.S. Mahmoudi, Thermoeconomic analysis & optimization of the combined supercritical CO2 (carbon dioxide) recompression Brayton/organic Rankine cycle, Energy 78 (2014) 501–512, https://doi.org/10.1016/j.energy.2014.10.037.

[14] S. Wright, P. Jr, A. Suo-Anttila, A. Al Rashdan, P. Tsvetkov, M. Vernon, D. Fleming, G. Rochau, Supercritical CO2 direct cycle gas fast reactor (SC-gfr) concept, ASME 2011 small modular reactors symposium, SMR (Somatosens. Mot. Res.) 2011 (2011), https://doi.org/10.2172/1013226.

[15] Y. Ahn, S.J. Bae, M. Kim, S.K. Cho, S. Baik, J.I. Lee, J.E. Cha, Review of supercritical CO2 power cycle technology and current status of research and development, Nucl. Eng. Technol. 47 (2015) 647–661, https://doi.org/10.1016/j.net.2015.06.009.

[16] V. Dostal, P. Hejzlar, M. Driscoll, The supercritical carbon dioxide power cycle: comparison to other advanced power cycles, Nucl. Technol. 154 (2006) 283–301, https://doi.org/10.13182/nt06-a3734.

[17] P. Hejzlar, V. Dostal, M.J. Driscoll, P. Dumaz, G. Poullennec, N. Alpy, Assessment of gas cooled fast reactor with indirect supercritical CO2 cycle, Nucl. Eng. Technol. 38 (2006) 109–118.

[18] G. Angelino, Carbon dioxide condensation cycles for power production, J. Eng. Power 90 (1968) 287–295, https://doi.org/10.1115/1.3609190.

[19] E.G. Feher, The supercritical thermodynamic power cycle, Energy Convers. 8 (1968) 85–90, https://doi.org/10.1016/0013-7480(68)90105-8.

[20] L. Chen, B. Deng, B. Jiang, X. Zhang, Thermal and hydrodynamic characteristics of supercritical CO2 natural circulation in closed loops, Nucl. Eng. Des. 257 (2013) 21–30, https://doi.org/10.1016/j.nucengdes.2013.01.016.

[21] V. Dostal, M.J. Driscoll, P. Hejzlar, N.E. Todreas, A supercritical CO2 gas turbine power cycle for next-generation nuclear reactors, in: International Conference on Nuclear Engineering, 2002, pp. 567–574.

[22] M. Li, H. Zhu, J. Guo, K. Wang, W. Tao, The development technology and applications of supercritical CO2 power cycle in nuclear energy, solar energy and other energy industries, Appl. Therm. Eng. 126 (2017) 255–275, https://doi.org/10.1016/j.applthermaleng.2017.07.173.

[23] H.S. Pham, N. Alpy, J.H. Ferrasse, O. Boutin, J. Quenaut, M. Tothill, D. Haubensack, M. Saez, Mapping of the thermodynamic performance of the supercritical CO2 cycle and optimisation for a small modular reactor and a sodium-cooled fast reactor, Energy 87 (2015) 412–424, https://doi.org/10.1016/j.energy.2015.05.022.

[24] H. Li, G. Fan, L. Cao, Y. Yang, X. Yan, Y. Dai, G. Zhang, J. Wang, A comprehensive investigation on the design and off-design performance of supercritical carbon dioxide power system based on the small-scale lead-cooled fast reactor, J. Clean. Prod. 256 (2020), 120720, https://doi.org/10.1016/j.jclepro.2020.120720.

[25] B.D. Iverson, T.M. Conboy, J.J. Pasch, A.M. Kruizenga, Supercritical CO2 Brayton cycles for solar-thermal energy, Appl. Energy 111 (2013) 957–970, https://doi.org/10.1016/j.apenergy.2013.06.020.

[26] S.M. Besarati, D.Y. Goswami, Analysis of advanced supercritical carbon dioxide power cycles with a bottoming cycle for concentrating solar power applications, J. Sol. Energ.-T. ASME 136 (2014), https://doi.org/10.1115/1.4025700.

[27] H. Qi, N. Gui, X. Yang, J. Tu, S. Jiang, The application of supercritical CO2 in nuclear engineering: a review, J. Comput. Multiph. Flows 10 (2018) 149–158, https://doi.org/10.1177/1757482X18765377.

[28] E. Guelpa, V. Verda, Exergoeconomic analysis for the design improvement of supercritical CO2 cycle in concentrated solar plant, Energy 206 (2020), 118024, https://doi.org/10.1016/j.energy.2020.118024.

[29] K. Sridharan, Corrosion of Structural Materials for Advanced Supercritical Carbon- Dioxide Brayton Cycle, Univ. of Wisconsin, Madison, WI (United States), 2017.

[30] R.P. Oleksak, F. Rouillard, Materials performance in CO2 and supercritical CO2, Comprehensive Nuclear Mater. (2020) 422–451, https://doi.org/10.1016/B978-0-12-803581-8.11622-4.

[31] L. Yang, H. Qian, W. Kuang, Corrosion behaviors of heat-resisting alloys in high temperature carbon dioxide, Materials 15 (2022) 1331, https://doi.org/10.3390/ma15041331.

[32] P. Dodds, Developing new reactors: learning the lessons of the past, Nucl. Energy 43 (2004) 331–336, https://doi.org/10.1680/nuen.43.6.331.55676.

[33] Y. Kim, H. Jang, Y. Oh, High temperature low cycle fatigue properties of a HF30-type cast austenitic stainless steel, Mater. Sci. Eng., A 526 (2009) 244–249, https://doi.org/10.1016/j.msea.2009.07.044.

[34] S. Xu, X.Q. Wu, E.H. Han, W. Ke, Y. Katada, Crack initiation mechanisms for low cycle fatigue of type 316Ti stainless steel in high temperature water, Mater. Sci. Eng., A 490 (2008) 16–25, https://doi.org/10.1016/j.msea.2007.12.043.

[35] H. Sun, X. Wu, E. Han, Y. Wei, Effects of pH and dissolved oxygen on electrochemical behavior and oxide films of 304SS in borated and lithiated high temperature water, Corrosion Sci. 59 (2012) 334–342, https://doi.org/10.1016/j.corsci.2012.03.022.

[36] H. Sun, X. Wu, E. Han, Effects of temperature on the oxide film properties of 304 stainless steel in high temperature lithium borate buffer solution, Corrosion Sci. 51 (2009) 2840–2847, https://doi.org/10.1016/j.corsci.2009.08.006.

[37] W. Karlsen, G. Diego, B. Devrient, Localized deformation as a key precursor to initiation of intergranular stress corrosion cracking of austenitic stainless steels employed in nuclear power plants, J. Nucl. Mater. 406 (2010) 138–151, https://doi.org/10.1016/j.jnucmat.2010.01.029.

[38] J.K.L. Lai, C.H. Shek, K.H. Lo, Stainless Steels: an Introduction and Their Recent Developments, Bentham Science Publishers, 2012.

[39] Y. Gui, Z. Liang, Q. Zhao, Corrosion and carburization behavior of heat-resistant steels in a high-temperature supercritical carbon dioxide environment, Oxid. Metals 92 (2019) 123–136, https://doi.org/10.1007/s11085-019-09917-x.

[40] Z. Zhu, Y. Cheng, B. Xiao, H.I. Khan, H. Xu, N. Zhang, Corrosion behavior of ferritic and ferritic-martensitic steels in supercritical carbon dioxide, Energy 175 (2019) 1075–1084, https://doi.org/10.1016/j.energy.2019.03.146.

[41] T. Furukawa, Y. Inagaki, M. Aritomi, Compatibility of FBR structural materials with supercritical carbon dioxide, Prog. Nucl. Energy 53 (2011) 1050–1055, https://doi.org/10.1016/j.pnucene.2011.04.030.

[42] H.J. Lee, H. Kim, S.H. Kim, C. Jang, Corrosion and carburization behavior of chromia-forming heat resistant alloys in a high-temperature supercritical-carbon dioxide environment, Corrosion Sci. 99 (2015) 227–239, https://doi.org/10.1016/j.corsci.2015.07.007.

[43] R.I. Olivares, D.J. Young, P. Marvig, W. Stein, Alloys SS316 and Hastelloy-C276 in supercritical CO2 at high temperature, Oxid. Metals 84 (2015) 585–606, https://doi.org/10.1007/s11085-015-9589-5.

[44] R.P. Oleksak, J.P. Baltrus, J. Nakano, A. Nakano, G.R. Holcomb, Ö.N. Doğan, Mechanistic insights into the oxidation behavior of Ni alloys in high-temperature CO2, Corrosion Sci. 125 (2017) 77–86, https://doi.org/10.1016/j.corsci.2017.06.005.

[45] Z. Liang, Y. Gui, Y. Wang, Q. Zhao, Corrosion performance of heat-resisting steels and alloys in supercritical carbon dioxide at 650 °C and 15 MPa, Energy 175 (2019) 345–352, https://doi.org/10.1016/j.energy.2019.03.014.

[46] Y. Gui, Z. Liang, H. Shao, Q. Zhao, Corrosion behavior and lifetime prediction of VM12, Sanicro 25 and Inconel 617 in supercritical carbon dioxide at 600 °C, Corrosion Sci. 175 (2020), 108870, https://doi.org/10.1016/j.corsci.2020.108870.

[47] G.R. Holcomb, C. Carney, Ö.N. Doğan, P.P.M.W. National Energy Technology Laboratory Netl, Oxidation of alloys for energy applications in supercritical CO2 and H2O, Corrosion Sci. 109 (2016) 22–35, https://doi.org/10.1016/j.corsci.2016.03.018.

[48] T. Conboy, S. Wright, J. Pasch, D. Fleming, G. Rochau, R. Fuller, Performance characteristics of an operating supercritical CO2 Brayton cycle, J. Eng. Gas Turbines Power (2012), https://doi.org/10.1115/gt2012-68415.

[49] M.A. Pope, Thermal Hydraulic Design of a 2400 MW Th Direct Supercritical CO_2-cooled Fast Reactor, Massachusetts Institute of Technology, 2008.

[50] Muto, Ishiyama, Kato, Ishizuka, Aritomi, Application of supercritical CO2 gas turbine for the fossil fired thermal plant, J. Energy Power Eng. (2009) 415–420, https://doi.org/10.1299/jsmeicope.2009.2._2-415_.

[51] J.P. Gibbs, Corrosion of Various Engineering Alloys in Supercritical Carbon Dioxide, Massachusetts Institute of Technology, 2010.

[52] T. Furukawa, Y. Inagaki, M. Aritomi, Corrosion behavior of FBR structural materials in high temperature supercritical carbon dioxide, J. Power and Energy Syst. 4 (2010) 252–261, https://doi.org/10.1299/jpes.4.252.

[53] L. Tan, M. Anderson, D. Taylor, T.R. Allen, O.R.T.U. Oak Ridge National Lab. ORNL, Corrosion of austenitic and ferritic-martensitic steels exposed to supercritical carbon dioxide, Corrosion Sci. 53 (2011) 3273–3280, https://doi.org/10.1016/j.corsci.2011.06.002.

[54] F. Rouillard, F. Charton, G. Moine, Corrosion Behavior of Different Metallic Materials in Supercritical Carbon Dioxide at 550 Degrees C and 250 Bars, Corrosion, 2011, p. 67, https://doi.org/10.5006/1.3628683.

[55] F. Rouillard, G. Moine, L. Martinelli, J.C. Ruiz, Corrosion of 9Cr steel in CO2 at intermediate temperature I: mechanism of void-induced duplex oxide formation, Oxid. Metals 77 (2012) 27–55, https://doi.org/10.1007/s11085-011-9271-5.

[56] G. Cao, V. Firouzdor, K. Sridharan, M. Anderson, T.R. Allen, Corrosion of austenitic alloys in high temperature supercritical carbon dioxide, Corrosion Sci. 60 (2012) 246–255, https://doi.org/10.1016/j.corsci.2012.03.029.

[57] V. Firouzdor, K. Sridharan, G. Cao, M. Anderson, T.R. Allen, Corrosion of a stainless steel and nickel-based alloys in high temperature supercritical carbon dioxide environment, Corrosion Sci. 69 (2013) 281–291, https://doi.org/10.1016/j.corsci.2012.11.041.

[58] T. Furukawa, F. Rouillard, Oxidation and carburizing of FBR structural materials in carbon dioxide, Prog. Nucl. Energy 82 (2015) 136–141, https://doi.org/10.1016/j.pnucene.2014.07.038.

[59] H.J. Lee, G.O. Subramanian, S.H. Kim, C. Jang, Effect of pressure on the corrosion and carburization behavior of chromia-forming heat-resistant alloys in high-temperature carbon dioxide environments, Corrosion Sci. 111 (2016) 649–658, https://doi.org/10.1016/j.corsci.2016.06.004.

[60] F. Rouillard, T. Furukawa, Corrosion of 9-12Cr ferritic–martensitic steels in high-temperature CO2, Corrosion Sci. 105 (2016) 120–132, https://doi.org/10.1016/j.corsci.2016.01.009.

[61] B.A. Pint, R.G. Brese, J.R. Keiser, O.R.T.U. Oak Ridge National Lab. ORNL, Effect of pressure on supercritical CO2 compatibility of structural alloys at 750 °C, Mater. Corros. 68 (2017) 151–158, https://doi.org/10.1002/maco.201508783.

[62] Z. Liang, M. Yu, Y. Gui, Q. Zhao, Corrosion behavior of heat-resistant materials in high-temperature carbon dioxide environment, JOM-US 70 (2018) 1464–1470, https://doi.org/10.1007/s11837-018-2975-0.

[63] S.H. Kim, G. Obulan Subramanian, C. Kim, C. Jang, K.M. Park, Surface modification of austenitic stainless steel for corrosion resistance in high temperature supercritical-carbon dioxide environment, Surf. Coating. Technol. 349 (2018) 415–425, https://doi.org/10.1016/j.surfcoat.2018.06.014.

[64] H.J. Lee, S.H. Kim, C. Jang, Characterization of Alloy 600 joints exposed to a high-temperature supercritical-carbon dioxide environment, Mater. Char. 138 (2018) 245–254, https://doi.org/10.1016/j.matchar.2018.02.025.

[65] H. Chen, S.H. Kim, C. Kim, J. Chen, C. Jang, Corrosion behaviors of four stainless steels with similar chromium content in supercritical carbon dioxide environment at 650 °C, Corrosion Sci. 156 (2019) 16–31, https://doi.org/10.1016/j.corsci.2019.04.043.

[66] A. Brittan, J. Mahaffey, M. Anderson, A.N.U.S. Sandia National Lab. SNL-NM, Corrosion and mechanical performance of grade 92 ferritic-martensitic steel after exposure to supercritical carbon dioxide, Metall. Mater. Trans. A 51 (2020) 2564–2572, https://doi.org/10.1007/s11661-020-05691-7.

[67] M.H.S. Bidabadi, Y. Zheng, A. Rehman, L. Yang, C. Zhang, H. Chen, Z. Yang, Effect of CO2 gas pressure on composition, growth rate, and structure of duplex oxide formed on 9Cr steel at 550 °C, Corrosion Sci. 163 (2020), 108252, https://doi.org/10.1016/j.corsci.2019.108252.

[68] H. Yang, W. Liu, B. Gong, E. Jiang, Y. Huang, G. Zhang, Y. Zhao, Corrosion behavior of typical structural steels in 500 °C, 600 °C and high pressure supercritical carbon dioxide conditions, Corrosion Sci. 192 (2021), 109801, https://doi.org/10.1016/j.corsci.2021.109801.

[69] A. Brittan, J. Mahaffey, D. Adam, M. Anderson, A.N.U.S. Sandia National Lab. SNL-NM, Mechanical and corrosion response of 316SS in supercritical CO2, Oxid. Metals 95 (2021) 409–425, https://doi.org/10.1007/s11085-021-10026-x.

[70] D. Huenert, A. Kranzmann, Impact of oxyfuel atmospheres H2O/CO2/O2 and H2O/CO2 on the oxidation of ferritic–martensitic and austenitic steels, Corrosion Sci. 53 (2011) 2306–2317, https://doi.org/10.1016/j.corsci.2011.03.015.

[71] J. Mahaffey, A. Kalra, M. Anderson, K. Sridharan, Materials corrosion in high temperature supercritical carbon dioxide, in: 4th International Symposium-Supercritical CO2 Power Cycles, Citeseer, 2014.

[72] T.D. Nguyen, J. Zhang, D.J. Young, Effects of cerium and manganese on corrosion of Fe–Cr and Fe–Cr–Ni alloys in Ar–20CO2 and Ar–20CO2–20H2O gases at 650°C, Corrosion Sci. 100 (2015) 448–465, https://doi.org/10.1016/j.corsci.2015.08.012.

[73] T.D. Nguyen, J. Zhang, D.J. Young, Water vapor effects on corrosion of Fe–Cr and Fe–Cr–Ni alloys containing silicon in CO2 gas at 818 °C, Oxid. Metals 83 (2015) 575–594, https://doi.org/10.1007/s11085-015-9536-5.

[74] J. Mahaffey, D. Adam, A. Brittan, M. Anderson, K. Sridharan, M.W.U.S. Univ. Of Wisconsin, L.U.S. Alliance For Sustainable Energy, Corrosion of alloy Haynes 230 in high temperature supercritical carbon dioxide with oxygen impurity additions, Oxid. Metals 86 (2016) 567–580, https://doi.org/10.1007/s11085-016-9654-8.

[75] J. Mahaffey, A. Schroeder, D. Adam, A. Brittan, M. Anderson, A. Couet, K. Sridharan, M.W.U.S. Univ. Of Wisconsin, L.U.S. Alliance For Sustainable Energy, Effects of CO and O2 impurities on supercritical CO2 corrosion of alloy 625, Metall. Mater. Trans. A 49 (2018) 3703–3714, https://doi.org/10.1007/s11661-018-4727-8.

[76] B.A. Pint, K.A. Unocic, The effect of CO2 pressure on chromia scale microstructure at 750°C, JOM-US 70 (2018) 1511–1519, https://doi.org/10.1007/s11837-018-2963-4.

[77] R.I. Olivares, D.J. Young, T.D. Nguyen, P. Marvig, Resistance of high-nickel, heat-resisting alloys to air and to supercritical CO2 at high temperatures, Oxid. Metals 90 (2018) 1–25, https://doi.org/10.1007/s11085-017-9820-7.

[78] R.P. Oleksak, J.H. Tylczak, C.S. Carney, G.R. Holcomb, O.N. Dogan, High-temperature oxidation of commercial alloys in supercritical CO2 and related power cycle environments, JOM-US 70 (2018) 1527–1534, https://doi.org/10.1007/s11837-018-2952-7.

[79] R.P. Oleksak, J.H. Tylczak, G.R. Holcomb, Ö.N. Doğan, P.P.M.W. National Energy Technology Laboratory Netl, High temperature oxidation of Ni alloys in CO2 containing impurities, Corrosion Sci. 157 (2019) 20–30, https://doi.org/10.1016/j.corsci.2019.05.019.

[80] B.A. Pint, J. Lehmusto, M.J. Lance, J.R. Keiser, Effect of pressure and impurities on oxidation in supercritical CO2, Mater. Corros. 70 (2019) 1400–1409, https://doi.org/10.1002/maco.201810652.

[81] Y. Gui, Z. Liang, S. Wang, Q. Zhao, Corrosion behavior of T91 tubing in high temperature supercritical carbon dioxide environment, Corrosion Sci. 211 (2023), 110857.

[82] J. Lehmusto, J.M. Kurley, M.J. Lance, J.R. Keiser, B.A. Pint, The impact of impurities on alloy behavior in supercritical CO2 at 700 °C, Oxid. Metals 94 (2020), https://doi.org/10.1007/s11085-020-09980-9.

[83] Y. Xie, J. Zhang, D.J. Young, Effects of Fe on oxidation of Ni-20Cr and Ni-30Cr alloys at 800 degrees C in wet CO(2)Gas, Oxid. Metals 94 (2020) 219–233, https://doi.org/10.1007/s11085-020-09987-2.

[84] R.P. Oleksak, J.H. Tylczak, G.R. Holcomb, Ö.N. Doğan, High temperature oxidation of steels in CO2 containing impurities, Corrosion Sci. 164 (2020), 108316, https://doi.org/10.1016/j.corsci.2019.108316.

[85] S.H. Kim, J. Cha, C. Jang, Corrosion and creep behavior of a Ni-base alloy in supercritical-carbon dioxide environment at 650 °C, Corrosion Sci. 174 (2020), 108843, https://doi.org/10.1016/j.corsci.2020.108843.

[86] S.R. Akanda, R.P. Oleksak, R. Repukaiti, K.A. Rozman, Ö.N. Doğan, Effect of specimen thickness on the degradation of mechanical properties of ferritic-martensitic P91 steel by direct-fired supercritical CO2 power cycle environment, Metall. Mater. Trans. 52 (2020) 82–93, https://doi.org/10.1007/s11661-020-06065-9.

[87] K. Li, Y. Zeng, J. Luo, Corrosion of SS310 and Alloy 740 in high temperature supercritical CO2 with impurities H2O and O2, Corrosion Sci. 184 (2021), 109350, https://doi.org/10.1016/j.corsci.2021.109350.

[88] K.A. Rozman, R.P. Oleksak, Ö.N. Doğan, M. Detrois, P.D. Jablonski, J.A. Hawk, Creep of MARBN-type 9Cr martensitic steel in gaseous CO2 environment, Mater. Sci. Eng., A 826 (2021), 141996, https://doi.org/10.1016/j.msea.2021.141996.

[89] H. Pei, M. Li, P. Wang, X. Yao, Z. Wen, Z. Yue, The effect of tensile stress on oxidation behavior of nickel-base single crystal superalloy, Corrosion Sci. 191 (2021), 109737, https://doi.org/10.1016/j.corsci.2021.109737.

[90] M. Cox, B. McEnaney, V.D. Scott, Vacancy condensation and void formation in duplex oxide scales on alloys, Philos. Mag. A 28 (1973) 309–319, https://doi.org/10.1080/14786437308217455.

[91] M. Cox, B. McEnaney, V.D. Scott, Diffusion and partitioning of elements in oxide scales on alloys, Nat. Phys. Sci. (Lond.) 237 (1972) 140–142, https://doi.org/10.1080/14786437208226960.

[92] P.L. Harrison, R.B. Dooley, S.K. Lister, D.B. Meadowcroft, P.J. Nolan, R.E. Pendlebury, P.L. Surman, M.R. Wootton, Oxidation of 9Cr–1Mo Steels in Carbon Dioxide. Discussion of Possible Mechanisms, Thomas Telford, 1974.

[93] B.A. Pint, R. Pillai, M.J. Lance, J.R. Keiser, Effect of pressure and thermal cycling on long-term oxidation in CO2 and supercritical CO2, Oxid. Metals 94 (2020) 505–526, https://doi.org/10.1007/s11085-020-10004-9.

[94] G.O. Subramanian, H.J. Lee, S.H. Kim, C. Jang, Corrosion and carburization behaviour of Ni-xCr binary alloys in a high-temperature supercritical-carbon dioxide environment, Oxid. Metals 89 (2017) 683–697, https://doi.org/10.1007/s11085-017-9811-8.

[95] B. Xiao, N. Zhang, K. Li, Z. Zhu, T. Zhang, M. Zhou, Corrosion behaviour of Ni-based alloy Inconel 740H in supercritical carbon dioxide at 650–700°C, Corrosion Engineering, Sci. Technol. 58 (2023) 180–189, https://doi.org/10.1080/1478422X.2022.2157534.

[96] M. Vamshi, S.K. Singh, N. Sateesh, D.S. Nagaraju, R. Subbiah, A review on influence of carburizing on ferritic stainless steel, Mater. Today: Proc. 26 (2020) 937–943, https://doi.org/10.1016/j.matpr.2020.01.151.

[97] G. Obulan Subramanian, S.H. Kim, C. Jang, The carburization behavior of alloy 800HT in high temperature supercritical-CO2, Mater. Lett. 299 (2021), 130067, https://doi.org/10.1016/j.matlet.2021.130067.

[98] D.J. Young, T.D. Nguyen, P. Felfer, J. Zhang, J.M. Cairney, Penetration of protective chromia scales by carbon, Scripta Mater. 77 (2014) 29–32, https://doi.org/10.1016/j.scriptamat.2014.01.009.

[99] H.J. Lee, S.H. Kim, H. Kim, C. Jang, Corrosion and carburization behavior of Al-rich surface layer on Ni-base alloy in supercritical-carbon dioxide environment, Appl. Surf. Sci. 388 (2016) 483–490, https://doi.org/10.1016/j.apsusc.2015.11.162.

[100] Y. Zhang, K. Gao, G. Schmitt, Water Effect on Steel under Supercritical CO2 Condition, NACE - International Corrosion Conference Series, 2011.

[101] J. Tan, K.S. Chan, Understanding Advanced Physical Inorganic Chemistry: the Learner's Approach, World Scientific Publishing Company, 2010.

[102] G. Cui, Z. Yang, J. Liu, Z. Li, A comprehensive review of metal corrosion in a supercritical CO2 environment, Int. J. Greenh. Gas Control 90 (2019), 102814, https://doi.org/10.1016/j.ijggc.2019.102814.

[103] T.D. Nguyen, Y. Xie, S. Ding, J. Zhang, D.J. Young, Oxidation behavior of Ni–Cr alloys in CO2 at 700 °C, Oxid. Metals 87 (2017) 605–616, https://doi.org/10.1007/s11085-017-9721-9.

[104] Y. Xie, J. Zhang, D.J. Young, Temperature effect on oxidation behavior of Ni-Cr alloys in CO2 gas atmosphere, J. Electrochem. Soc. 164 (2017) C285–C293, https://doi.org/10.1149/2.1021706jes.

[105] Y. Liu, G. Xiao, M. Wang, Q. Guo, Z. Wang, Y. Wu, H. Xu, D. Chen, Corrosion behavior of heat-resistant steel T91 in high-temperature supercritical carbon dioxide with impurity O2, SO2 or H2S, J. Supercrit. Fluids 198 (2023), 105936, https://doi.org/10.1016/j.supflu.2023.105936.

[106] R.P. Oleksak, C.S. Carney, Ö.N. Doğan, Effect of pressure on high-temperature oxidation of Ni alloys in supercritical CO2 containing impurities, Corrosion Sci. 215 (2023), 111055, https://doi.org/10.1016/j.corsci.2023.111055.

[107] R.P. Oleksak, J.H. Tylczak, Ö.N. Doğan, Temperature-dependence of oxidation and carburization of Grade 91 steel in CO2 containing impurities, Corrosion Sci. 198 (2022), 110147, https://doi.org/10.1016/j.corsci.2022.110147.

[108] Y. Xiang, M. Xu, Y. Choi, State-of-the-art overview of pipeline steel corrosion in impure dense CO2 for CCS transportation: mechanisms and models, Corrosion Eng. Sci. Technol. 52 (2017) 485–509, https://doi.org/10.1080/1478422X.2017.1304690.

[109] L. Wei, X. Pang, C. Liu, K. Gao, Formation mechanism and protective property of corrosion product scale on X70 steel under supercritical CO2 environment, Corrosion Sci. 100 (2015) 404–420, https://doi.org/10.1016/j.corsci.2015.08.016.

[110] M. Banaszkiewicz, A. Rehmus-Forc, Stress corrosion cracking of a 60 MW steam turbine rotor, Eng. Fail. Anal. 51 (2015) 55–68, https://doi.org/10.1016/j.engfailanal.2015.02.015.

[111] Y. Wei, Y. Li, J. Lai, Q. Zhao, Z. Lin, Analysis on corrosion fatigue cracking mechanism of 17-4PH blade of low pressure rotor of steam turbine, Eng. Fail. Anal. 118 (2020), 104925, https://doi.org/10.22541/au.158379423.39702389.

[112] R.F. Domagala, High-temperature Creep Evaluation in Carbon Dioxide Atmosphere, Summary Report, 1961.

[113] W.R. Martin, H.E. McCoy, Effect of CO2 on the strength and ductility of type 304 stainless steel at elevated temperatures, Corrosion (Houston, TX, U. S.) 19 (5) (1963) 157t–164t, https://doi.org/10.5006/0010-9312-19.5.157.